J. Fluid Mech. (2023), *vol*. 958, A31, doi:10.1017/jfm.2023.102

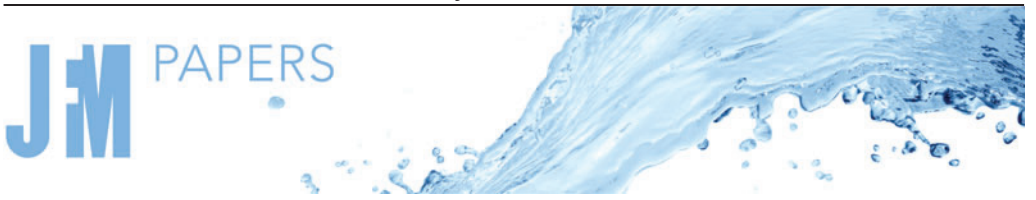

Entrainment mechanism of turbulent synthetic jet flow

Congyi Xu[1], **Yanguang Long**[1] **and Jinjun Wang**[1,†]

[1]Fluid Mechanics Key Laboratory of Education Ministry, Beihang University, Beijing 100191, PR China

(Received 9 August 2022; revised 2 December 2022; accepted 29 January 2023)

Synthetic jets have received extensive attention due to their superior mixing property. However, its mechanisms have not been investigated from the perspective of the turbulent/non-turbulent interface (TNTI). To shed new light on this issue, the entrainment and TNTI properties of a synthetic jet are experimentally investigated and compared with a continuous jet at $Re_j = 3150$. The fuzzy clustering method is applied to select an appropriate vorticity threshold to detect the TNTI. Statistically, it is revealed that the entrainment coefficients of the two jets significantly differ in the near field, while they become almost identical in the far field. Instead of the vortex ring, the 'breakdown of the vortex ring' enhances the entrainment in the present synthetic jet. Instantaneously, the TNTI more violently fluctuates in the near field of the synthetic jet, which leads to a larger fluctuation in the TNTI radial position, a higher fractal dimension and enhanced local entrainment. Moreover, the transition of the probability density function of the TNTI orientation from the unimodal distribution in the near field to the bimodal distribution in the far field is found in both jets. The multi-scale analysis reveals a new mechanism for the bimodal distribution caused by the TNTI-thickness-scale structures.

Key words: jets, turbulent mixing, mixing enhancement

1. Introduction

The synthetic jet is a discontinuous jet produced by the actuator periodically blowing and sucking the environment fluid (Glezer & Amitay 2002). The fluid blown by the actuator from the orifice/slot forms vortex rings/pairs due to shear and moves downstream under its self-induced velocity. As a new type of active flow control technology, synthetic jets have attracted extensive attention due to their advantages such as the lack of an external air source and the simple actuator structure, and they have been applied in the fields of fluid mixing (Eri *et al.* 2016; Zhang *et al.* 2021*a*) and active flow control (Zong, van Pelt & Kotsonis 2018; Cao *et al.* 2019).

† Email address for correspondence: jjwang@buaa.edu.cn

Since the concept of a synthetic jet was proposed (James, Jacobs & Glezer 1996; Smith & Glezer 1998), a great deal of research has focused on its properties. The flow produced by a synthetic jet actuator with a circular orifice was studied by Mallinson, Hong & Reizes (1999); Mallinson, Reizes & Hong (2001) through experiments and numerical simulations. The synthetic jet more rapidly reaches self-similarity than the continuous jet, which they attributed to the stronger velocity fluctuation in the synthetic jet. Furthermore, synthetic jets and continuous jets with identical Reynolds number were experimentally studied by Smith & Swift (2003). The results show that synthetic jets exhibit a larger growth rate of volumetric flow in the near field, and the value is close to that of continuous jets in the far field. They attributed the greater entrainment to the roll-up of the synthetic jet vortex pair. Similarly, Shuster & Smith (2007) found that the spreading rates of the synthetic jet were almost twice those of the continuous jet, which indicates that the entrainment of the synthetic jet was greater. The greater entrainment of synthetic jets can improve the mixing (Eri *et al.* 2016; Zhang *et al.* 2021*a*), heat transfer (Krishan, Aw & Sharma 2019) and other performance in engineering applications.

In recent years, the study of the turbulent/non-turbulent interface (TNTI) has provided new ideas to investigate entrainment mechanisms. The TNTI is a very thin layer of fluids that separates turbulent and non-turbulent regions in the instantaneous flow (da Silva *et al.* 2014*a*). The entrainment can be characterized by the transport of non-turbulent fluid across the TNTI (Mistry *et al.* 2016). The entrainment process can be visually divided into two parts: engulfment and nibbling (Jahanbakhshi & Madnia 2016; Mistry *et al.* 2016; Breda & Buxton 2019). The former refers to the process where the environment irrotational fluid is drawn into the turbulent region by inviscid motion, and the latter refers to the vorticity propagation process that occurs along the TNTI (Jahanbakhshi & Madnia 2016). Both processes are affected by the flow near the TNTI.

The geometric properties of TNTIs are related to the local entrainment. Mistry, Philip & Dawson (2019) evaluated the conditional average entrainment velocity based on the geometric properties of local TNTIs in a high-Reynolds-number continuous jet. They found that the great local entrainment was statistically accompanied by the TNTI whose radial position is near the jet centreline, the surface curvature is convex and the position is at the 'leading edges' of the TNTI. By comparing circular and fractal orifice jets, Breda & Buxton (2018, 2019) found that the fractal orifice suppresses large-scale coherent structures in the near field of the jet. In this region, the TNTI of the fractal orifice jet exhibits a smaller radial position fluctuation and a smoother shape. They suggested that the more frequent large-scale excursions of the TNTI in the circular orifice jet enhanced the engulfment process, and the more distorted geometry enhanced the nibbling process, which may be the reason for its greater entrainment. In their study of a fully developed turbulent mixing layer, Balamurugan *et al.* (2020) found that the probability density function (p.d.f.) of the TNTI orientation exhibited a bimodal distribution, and the peaks appeared at approximately -50° and -130°. The conditional average vector field indicates the presence of two vortices at the mean interface location on either side of the mixing layer. The angle between the line that connects the centres of the two vortices and the downstream direction is close to the angle that corresponds to the peak of the bimodal distribution of the TNTI orientation. They argued that the bimodal distribution was related to the large-scale inclined Kelvin–Helmholtz vortical motions in the mixing layer.

In addition, several studies have evaluated the contribution of engulfment during the entrainment process. Mathew & Basu (2002) studied the round jet by temporal direct numerical simulation (DNS) and used the Lagrangian method to trace the pathlines of fluid particles into the turbulent region. They found that the vorticity of fluid particles increased to the threshold near the TNTI instead of inside the turbulent region, and the

engulfment volume was much smaller than that of the turbulent region, which indicates that engulfment is not the dominant process of entrainment. Taveira *et al.* (2013) performed Lagrangian statistics on millions of particles in the DNS of a turbulent plane jet and found that less than 1 % of the particles from the non-turbulent region entered the irrotational bubble in the turbulent region, which indicates that engulfment is not significant for the planar jet. Westerweel *et al.* (2005, 2009) and Jahanbakhshi & Madnia (2016) estimated the contribution of engulfment by counting the probability of irrotational bubbles appearing in the turbulent region. The results showed that engulfment accounted for at most 10 % of the total mass flux.

These studies on the TNTI illustrated the importance of the geometric properties of the TNTI and its surrounding flow field for the entrainment process. Therefore, the TNTI can be used to explain the greater entrainment in synthetic jets. To the best of our knowledge, there is currently no study on the properties of the TNTI in synthetic jet flows. The purpose of this paper is to reveal the entrainment mechanism of the synthetic jet from the perspective of the TNTI. This paper is organized as follows. The experimental apparatus and particle image velocimetry (PIV) are presented in § 2. The entrainment of the synthetic jet from the perspective of the mean flow is investigated in § 3. The mechanism of entrainment enhancement from the point of view of an instantaneous TNTI is explored in § 4. Finally, the paper is concluded in § 5.

2. Experimental methods

2.1. *Apparatus*

Continuous and synthetic jets are generated by the continuous jet nozzle and synthetic jet actuator, respectively. The structure of the continuous jet nozzle is shown in figure 1(*a*). Seeded air flows through the honeycomb, screen and contraction section before entering the external environment from the orifice with diameter $D = 5$ mm. The flow rates are controlled by a mass flow controller with an uncertainty less than 1.5 %. The diameter and length of the honeycomb cell are 1.6 mm and 25.4 mm, respectively. The mesh size and wire diameter of the screen are 0.7 mm and 0.17 mm, respectively. The contraction section adopts the shift Witozinsky curve, and the contraction ratio is 9. The structure of the synthetic jet actuator is shown in figure 1(*b*). The thin brass shim with a glued piezo-ceramic element is installed between the top cover and the base and forms a cavity with the top cover. The cavity is linked to the external environment through the orifice. O-rings are used between the contact surfaces to prevent air leakage. The sinusoidal signal generated by the Tektronix AFG1062 signal generator is amplified by the Aigtek ATA-214 voltage amplifier and used to drive the diaphragm. The synthetic jet actuator cavity is 4 mm in height (H_c) and 46 mm in diameter (D_c), and the orifice is 3 mm in height (H) and 5 mm in diameter (D).

To measure the characteristics of the synthetic jet actuator, a HangHua CTA-02A hot-wire anemometer is used to measure the velocity at the orifice. The maximum orifice velocity U_{max} over an excitation cycle varying the driving frequency f is presented in figure 2(*a*). The peaks of U_{max} appear at approximately 500 and 1200 Hz. The U_{max} for varying peak-to-peak values of the voltage V_{pp} is presented in figure 2(*b*). When the driving frequency f is fixed, U_{max} linearly increases with V_{pp} in the present measurements. Then, the synthetic jet with a specific frequency and maximum velocity can be generated with the above frequency and voltage characteristics. In the present experiment, the driving frequency f is fixed at 500 Hz, and the driving voltage is adjusted to make

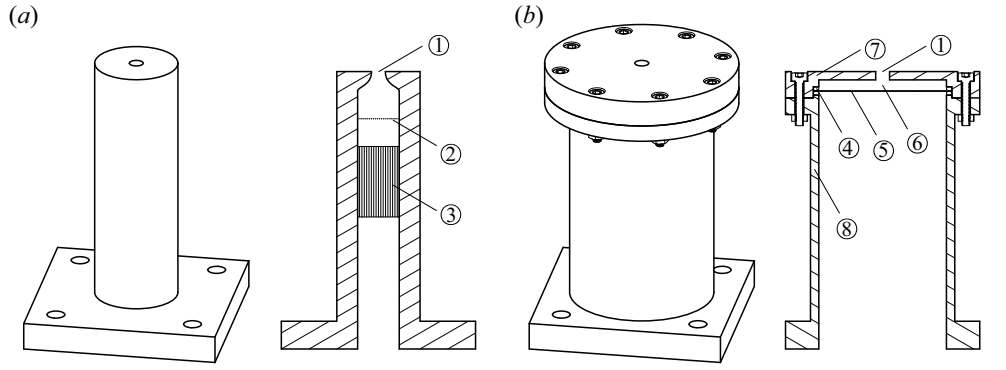

Figure 1. Schematic of the (*a*) continuous jet nozzle and (*b*) synthetic jet actuator. The symbols in the schematic are the (1) orifice, (2) screen, (3) honeycomb, (4) O-rings, (5) thin brass shim with a glued piezo-ceramic element, (6) cavity, (7) top cover and (8) base.

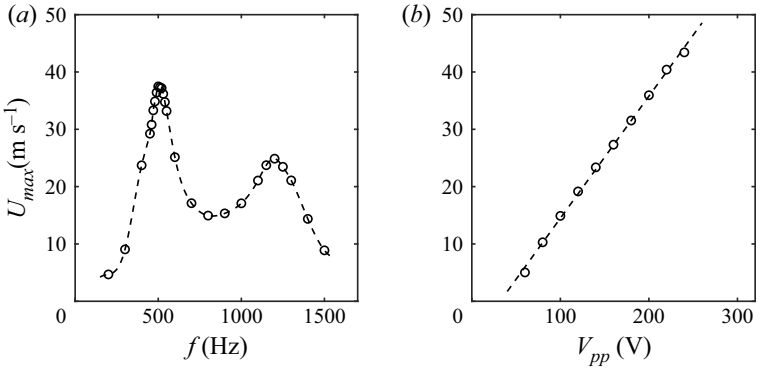

Figure 2. (*a*) Frequency characteristics of the synthetic jet actuator at $V_{pp} = 200$ V. (*b*) Voltage characteristics of the synthetic jet actuator at $f = 500$ Hz.

$U_{max} = 30\,\mathrm{m\,s^{-1}}$. Velocity $u_0(t)$ at the synthetic jet actuator orifice can be described by the following sine function:

$$u_0(t) = U_{max}\sin(2\pi ft). \tag{2.1}$$

The time-averaged blowing velocity over an excitation cycle (denoted by U_0) can be calculated from

$$U_0 = \frac{1}{T}\int_0^{T/2} u_0(t)\,\mathrm{d}t = \frac{U_{max}}{\pi}, \tag{2.2}$$

where $T = 1/f$ is the excitation period. The jet Reynolds number Re_j, which is based on U_0 and orifice diameter D, is defined as

$$Re_j = \frac{U_0 D}{\nu}, \tag{2.3}$$

where ν is the kinematic viscosity. The mean velocity of the continuous jet at the orifice is equal to U_0, and the two jets have identical Reynolds number $Re_j = 3150$. The definitions

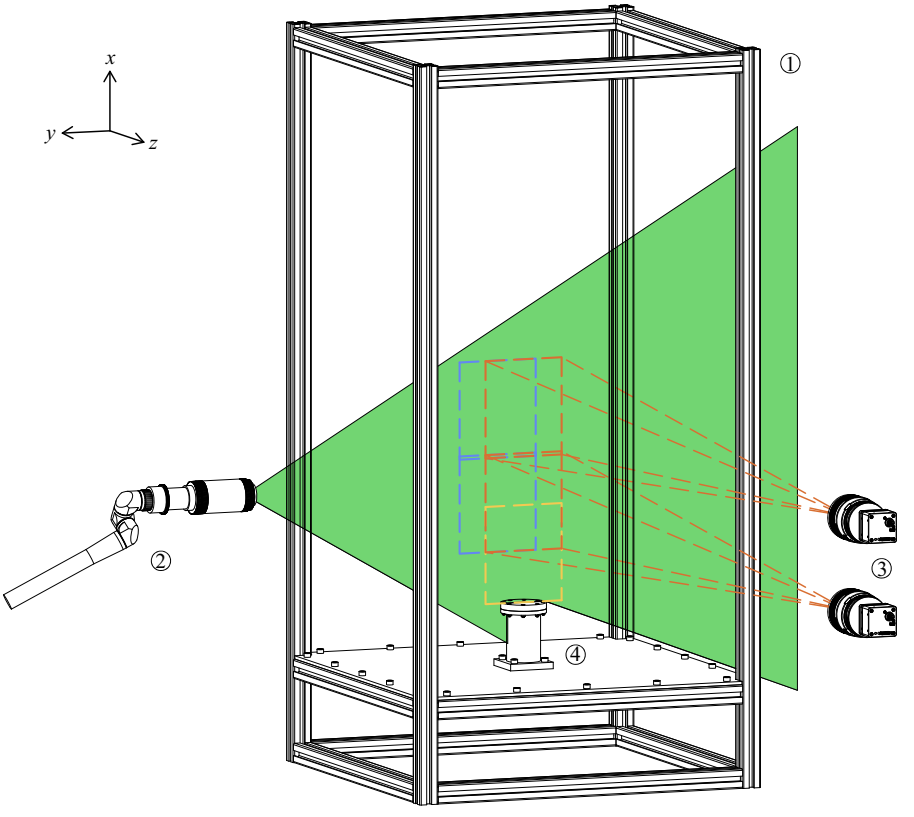

Figure 3. Schematic of the (1) container, (2) laser head connected to a light arm, (3) CCD cameras and (4) jet generator (continuous jet nozzle or synthetic jet actuator).

of parameters associated with the synthetic jet in the above equations make reference to previous works (Smith & Swift 2003; Shuster & Smith 2007).

2.2. *Particle image velocimetry measurement*

The two-dimensional (2-D) PIV experiments are conducted in a container with a size of 0.5 m × 0.5 m × 1 m, as shown in figure 3. The coordinate system is defined in figure 3, and the centre of the orifice is taken as the origin. The laser sheet produced by the Beamtech Vlite-380 Nd:YAG dual-cavity laser illuminates the x–y plane that passes through the centreline of the jet. CCD cameras (2456 × 2058 pixels) and Nikon 50 mm lenses are used to capture particle images. The sampling frequency is 5 Hz. Considering the limitation of the field of view and difference in flow velocity, the experiments are performed in three fields of view: FOV1, FOV2 and FOV3 (see figure 3 and table 1 for details). FOV2 and FOV3 are formed by splicing the fields of view of two cameras, and the overlapping width is approximately ten times the vector spacing to ensure reliable splicing results. The particle images are processed by the multi-pass iterative Lucas–Kanade algorithm (Champagnat *et al.* 2011; Pan *et al.* 2015) to obtain the velocity field. The uncertainty of particle displacement is approximately 0.1 pixels. Since the mean particle displacement in the present experiment is approximately 10 pixels, the uncertainty of the velocity field is approximately 1 %.

Experiment details	FOV1 (yellow)	FOV2 (red)	FOV3 (blue)
Range of FOV	$0 \leqslant x/D \leqslant 30$ $-12.5 \leqslant y/D \leqslant 12.5$	$16 \leqslant x/D \leqslant 75$ $-12.5 \leqslant y/D \leqslant 12.5$	$16 \leqslant x/D \leqslant 75$ $-4 \leqslant y/D \leqslant 21$
Interrogation window	32×32	32×32	32×32
Overlap	75 %	75 %	75 %
Num of Vectors	301×251	591×251	591×251
Vector Spacing	0.5 mm ($0.9\eta \sim 4.0\eta$)	0.5 mm ($0.5\eta \sim 2.5\eta$)	0.5 mm ($0.5\eta \sim 2.7\eta$)
Number of realizations	6000	6000	6000

Table 1. PIV experiment details.

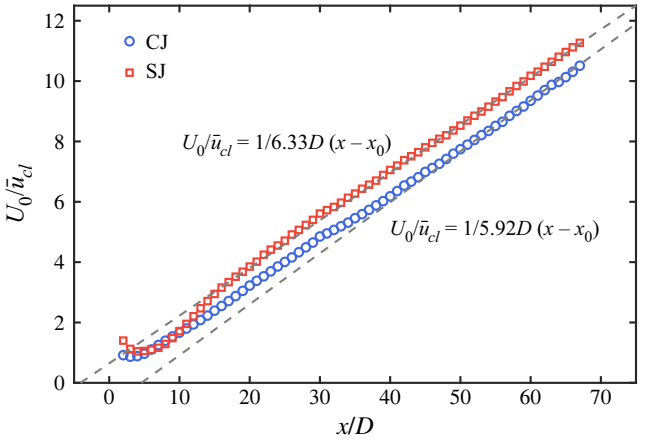

Figure 4. Inverse centreline velocity $\bar{u}_{cl}$ decay profile. In the legend, 'CJ' and 'SJ' represent the continuous jet and synthetic jet, respectively, and the meaning is identical in the subsequent figures.

3. Mean flow

3.1. *Flow characterization*

As shown in figure 4, the inverse of the centreline velocities of the continuous and synthetic jets linearly increases with the downstream distance for $x/D > 45$ and $x/D > 35$, respectively, following the equation (Pope 2000):

$$U_0/\bar{u}_{cl} = (x - x_0)/BD, \tag{3.1}$$

where B is the velocity-decay constant, and the overline represents the mean value over all snapshots. Here, $B = 5.92$ and 6.33 for the present continuous and synthetic jets, respectively. The values are consistent with those reported in previous studies (Panchapakesan & Lumley 1993; Hussein, Capp & George 1994; Mistry *et al.* 2016). In the near field, the centreline velocity of the synthetic jet more rapidly decays than that of the continuous jet, which indicates more violent mixing. The virtual origin x_0 is the imaginary location where the jet half-width approaches zero. Here, $x_0/D = 4.59$ and -4.09 for the present continuous and synthetic jets, respectively. The difference between the virtual origins is close to the difference between the positions where the inverse of the centreline velocities begins to linearly increase, which implies that the synthetic jet accelerates the flow evolution in the near field. To evaluate the influence range of the periodic flow structure of the synthetic jet, the proper orthogonal decomposition (POD) time coefficient is used to extract the phase information of the synthetic jet flow field

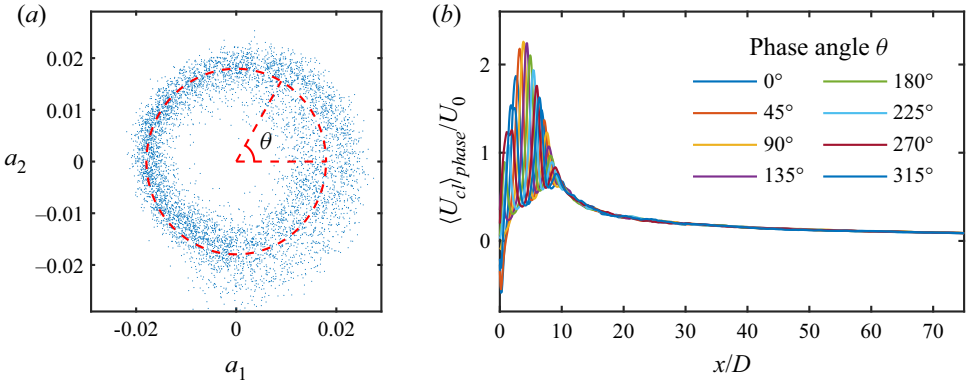

Figure 5. (*a*) Limit cycle formed by a_1 and a_2 of the synthetic jet flow field. (*b*) Phase-averaged centreline velocity $\langle u_{cl}\rangle_{phase}$ of the synthetic jet.

(Pan, Wang & Wang 2013). The method is suitable for low-sampling-rate measurement and can estimate the phase with sufficient accuracy for a much lower sampling rate than needed for the cross-correlation method. For a periodic/quasi-periodic flow field, the first several POD modes are dominant in the energy contribution. Time coefficients a_1 and a_2 that correspond to the first and second modes of the POD, respectively, loop around a limit cycle in the cross-plot a_1–a_2 plane, where every point represents one instantaneous snapshot. Based on the limit cycle, the phase information of the ith snapshot can be extracted by modelling the corresponding a_1^i and a_2^i as

$$\left.\begin{aligned} a_1^i &= r_i \sin(\theta_i), \\ a_2^i &= r_i \cos(\theta_i), \end{aligned}\right\} \tag{3.2}$$

where $r_i = \sqrt{(a_1^i)^2 + (a_2^i)^2}$, and θ_i is the phase angle. The limit cycle formed by a_1 and a_2 of the synthetic jet flow field is shown in figure 5(*a*). The phase-averaged value is defined as the mean value in the range of $\theta \pm 5°$, denoted by $\langle\cdot\rangle_{phase}$. Figure 5(*b*) shows the phase-averaged centreline velocity of the synthetic jet. There is almost no difference in the centreline velocity of different phases for $x/D > 10$, which indicates that the large-scale vortex structures near the orifice break down and lose their periodic characteristics. To more visually confirm this phenomenon, the phase-averaged λ_{ci} field of the synthetic jet over a period is shown in figure 6. The imaginary part of the complex eigenvalue pair of the velocity gradient tensor is denoted as λ_{ci} and can be referred to as the local swirling strength of the vortex (Zhou *et al.* 1999). Taking λ_{ci} as the criterion, the vortex ring evolution near the orifice of the synthetic jet can be visualized. The vortex ring is formed at the orifice and moves downstream under its self-induced velocity. Subsequently, the strength of the vortex ring decreases, its shape gradually becomes irregular and it breaks down at approximately $x/D = 10$. Figure 7 presents the normalized mean value and root mean square of the velocity profiles of the two jets. Both jets show good self-similarities for $x/D > 45$, which indicates that the flow fields are fully developed. Hereinafter, the regions with $x/D > 45$ are termed far fields, while the regions with $x/D < 45$ are classified as near fields. A comparison of figure 7(*c*) with figure 7(*d*) shows that the blowing and sucking of the synthetic jet cause larger streamwise velocity fluctuation near the orifice; then, the fluctuation nearly decreases to the value of the continuous jet in the far field. However, the streamwise

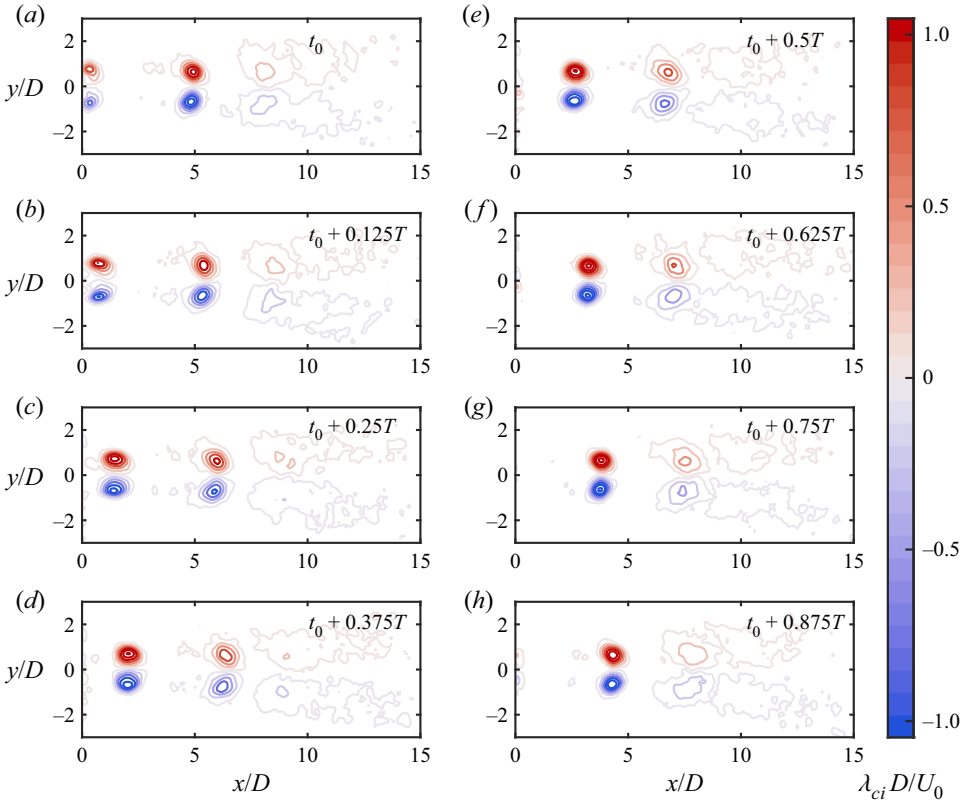

Figure 6. (*a–h*) Phase-averaged λ_{ci} field of the synthetic jet over a period. The sign of λ_{ci} is identical to the local vorticity.

velocity fluctuation near the orifice of the continuous jet is relatively small and gradually increases until it achieves self-similarity in the far field. For radial velocity fluctuation, similar conclusions can be obtained from figure 7(*e*,*f*). The slight asymmetry of the curve at $x/D = 75$ in figure 7(*c*) can be attributed to the poor image quality at the edge of the image and the attenuation of laser energy intensity. A similar asymmetry of the profile has also been observed in PIV measurements of a turbulent jet by Mistry *et al.* (2016). The slight asymmetry at the edge does not affect subsequent analysis.

3.2. *Entrainment analysis based on mean flow*

In this subsection, the entrainment characteristics of the synthetic jet will be analysed from the perspective of the mean flow. The time-averaged entrainment can be described by the growth rate of the jet half-width $\partial r_{1/2}/\partial x$, i.e. the spreading rate, and the volumetric flow rate Q^* (Cater & Soria 2002; Smith & Swift 2003; Breda & Buxton 2018). The half-widths of the two jets are presented in figure 8(*a*). The synthetic jet has a higher spreading rate than the continuous jet for $10 < x/D < 45$. In the far field, the spreading rates of both jets are close to 0.1, which is similar to previous studies (Panchapakesan & Lumley 1993; Hussein *et al.* 1994; Cater & Soria 2002; Mistry *et al.* 2016; Breda & Buxton 2017). Thus, the behaviours of the two jets are consistent after achieving self-similarity. The volumetric

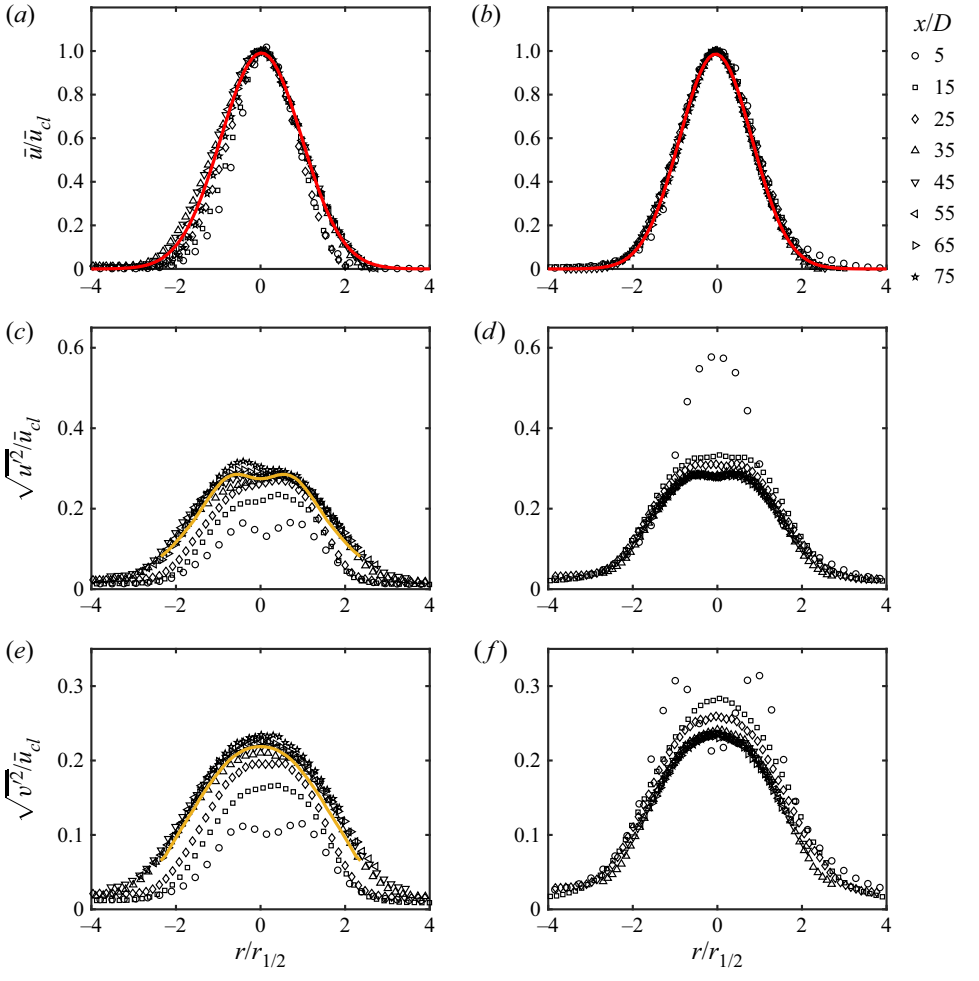

Figure 7. Profiles of the (*a*,*c*,*e*) continuous jet and (*b*,*d*,*f*) synthetic jet, normalized by the local centreline velocity $\bar{u}_{cl}$ and local jet half-width $r_{1/2}$. The jet half-width $r_{1/2}$ is measured as the radial distance from the centreline to the points where the mean velocity decays to half of the local centreline values. Mean profiles of the (*a*,*b*) streamwise velocity; root mean square profiles of the (*c*,*d*) axial velocity and (*e*,*f*) radial velocity. The red solid lines are the fitted Gaussian curves of the self-similar region. The yellow solid lines denote the self-similar profiles of the continuous jet reported by Hussein *et al.* (1994).

flow rate Q^* is defined as

$$Q^* = 2\pi \int_0^{r_0} \bar{u} r \, \mathrm{d}r, \tag{3.3}$$

where the integral boundary r_0 is the radial position of $\bar{u} = 0.02\bar{u}_{cl}$. This value is selected to be as small as possible after considering the field of view limitation and experimental noise. The synthetic jet has a higher volumetric flow rate than the continuous jet, as shown in figure 8(*b*). Thus, the synthetic jet has a greater entrainment, which is consistent with previous studies (Mallinson *et al.* 1999; Cater & Soria 2002; Smith & Swift 2003). The variation in entrainment coefficient α along the downstream direction is further analysed. The entrainment coefficient α quantifies entrainment of environmental fluid into the turbulent flow and represents the effect of turbulence on the mean flow

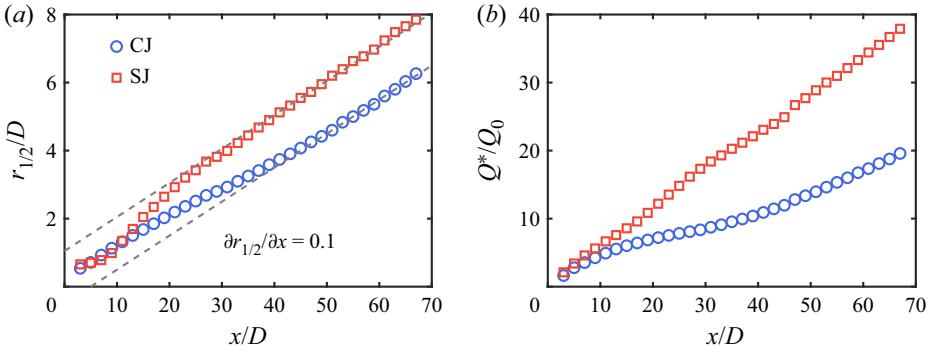

Figure 8. Variations in (*a*) half-width $r_{1/2}$ and (*b*) volumetric flow rate Q^*, normalized by D and $Q_0 = \pi D^2 U_0/4$, respectively. The grey dashed lines denote the slope of 0.1.

(Paillat & Kaminski 2014; van Reeuwijk & Craske 2015). van Reeuwijk & Craske (2015) considered an axisymmetric turbulent plume in cylindrical coordinate system and used the entrainment hypothesis of the form (Turner 1986):

$$-(rv)_{r=\infty} = \alpha r_m v_m, \tag{3.4}$$

where r and v are the radial direction and radial velocity, respectively, and r_m and v_m are the characteristic radius and velocity, respectively. The entrainment coefficient α, as a proportional coefficient, links the rate at which environment fluid is entrained into the plume and the typical velocity inside the plume. From the entrainment hypothesis 3.4 and the Reynolds-averaged conservation equation, the entrainment coefficient α can be derived as follows:

$$\alpha = -\frac{\delta_m}{2\gamma_m} + \frac{Q}{2M^{1/2}}\frac{\partial}{\partial x}(\ln \gamma_m) = \alpha_1 + \alpha_2. \tag{3.5}$$

The terms in (3.5) are given in table 2. The Richardson number Ri from the original equation has been set to zero to make it valid for a pure jet (Breda & Buxton 2018), and a detailed derivation is provided by van Reeuwijk & Craske (2015). The first term $\alpha_1 = -(\delta_m/2\gamma_m)$ is related to the production of turbulent kinetic energy, and the second term $\alpha_2 = (Q/2M^{1/2})(\partial/\partial x)(\ln \gamma_m)$ is related to the shape of the velocity profile. The variations in entrainment coefficient α and its components are shown in figure 9. The synthetic jet has a larger entrainment coefficient than the continuous jet in the near field, and it gradually decreases to a constant value, which is almost equal to that of the continuous jet in the far field. The constant value of approximately 0.11 is close to the entrainment coefficient of 0.057–0.109 for the pure jet and the plume that removes the influence of the buoyancy term (van Reeuwijk & Craske 2015). The entrainment coefficient of the synthetic jet is maximal for $10 < x/D < 15$. Combined with the above results of the centreline velocity, half-width and volumetric flow rate, the strongest entrainment of the present synthetic jet appears after the complete breakdown of the vortex ring. Unlike the previous view that the vortex ring promotes entrainment (Cater & Soria 2002; Smith & Swift 2003), the 'breakdown of the vortex ring' causes the entrainment enhancement in the present synthetic jet. As shown in figure 9, the difference in entrainment coefficient between the two jets is mainly contributed by α_1, which corresponds to the enhanced production of turbulent kinetic energy in the vortex ring breakdown process.

Term	Equation	Term	Equation
Mean volume flux	$Q = 2\int_0^{r_0} \bar{u} r \, \mathrm{d}r$	Characteristic jet velocity	$u_m = \dfrac{M}{Q}$
Mean momentum flux	$M = 2\int_0^{r_0} \bar{u}^2 r \, \mathrm{d}r$	Mean turbulence production	$\delta_m = \dfrac{4}{u_m^3 r_m}\int_0^{r_0} \overline{u'v'}\dfrac{\partial \bar{u}}{\partial r} r \, \mathrm{d}r$
Characteristic jet width	$r_m = \dfrac{Q}{M^{1/2}}$	Mean energy	$\gamma_m = \dfrac{2}{u_m^3 r_m^2}\int_0^{r_0} \bar{u}^3 r \, \mathrm{d}r$

Table 2. The terms in (3.5) (Breda & Buxton 2018).

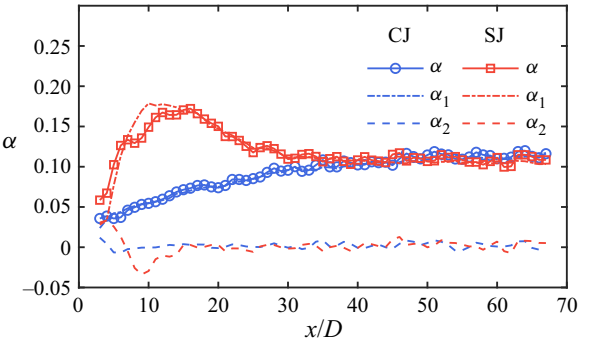

Figure 9. Variations of the entrainment coefficient α and its components.

4. Turbulent/non-turbulent interface: detection and properties

4.1. *TNTI detection method*

Before studying the TNTI of the synthetic jet, a suitable indicator scalar must be determined to detect the TNTI. Commonly used indicator scalars include the vorticity magnitude (Bisset, Hunt & Rogers 2002), spanwise vorticity magnitude (Balamurugan *et al.* 2020), turbulent kinetic energy (TKE) (Chauhan *et al.* 2014), homogeneity criterion (Reuther & Kahler 2018) and passive scalar (Westerweel *et al.* 2009), fluctuation of velocity along particle Lagrangian trajectory (Long, Wu & Wang 2021), etc. Considering the applicable conditions of these indicator scalars and the 2-D PIV data obtained in the present study, the spanwise vorticity magnitude $|\omega_z|$ is used as the indicator scalar. Regarding the use of $|\omega_z|$ as the indicator in experimental measurements, Watanabe, Zhang & Nagata (2018) compared the TNTI detected by $|\omega_z|$ and vorticity magnitude $|\omega|$ in the turbulent boundary layer, found that the TNTI detected by $|\omega_z|$ was almost identical to that detected by $|\omega|$ and concluded that like $|\omega|$, $|\omega_z|$ was a good marker for detecting turbulent fluids. Recent experimental studies on the turbulent mixing layer (Balamurugan *et al.* 2020) and turbulent boundary layer (Long *et al.* 2021) have used $|\omega_z|$ as the indicator, which proves the feasibility of using $|\omega_z|$ as the indicator in the shear flow dominated by streamwise velocity. According to Balamurugan *et al.* (2020), the relatively high spatial resolution provides an advantage for using $|\omega_z|$ for the TNTI detection. The spatial resolution of the present experiment is close to that of Balamurugan *et al.* (2020), and the $|\omega_z|$ indicator can be considered feasible in the present study. Due to numerical and experimental noise, the irrotational boundary of the TNTI must be determined by a very small but non-zero vorticity threshold. In previous numerical simulation studies, the

vorticity threshold is often selected in the 'neck region' of the joint p.d.f. of vorticity and vertical distance (Watanabe *et al.* 2018) or the 'plateau region' where the volume of the turbulent region decreases with the threshold with a small slope (Watanabe *et al.* 2015). However, in experimental data, such regions may not be obvious due to experimental noise; hence, it is difficult to select the threshold through empirical methods. The fuzzy clustering method (FCM), as an unsupervised machine learning algorithm, has been used to detect the TNTI in the turbulent boundary layer (Younes *et al.* 2021) and the airfoil flow (Zhang, Rival & Wu 2021*b*). Younes *et al.* (2021) assessed the FCM performance by comparison with the TKE method on three different experimental wall-bounded turbulent flow datasets, and the results show that FCM performs comparably to the TKE method. Zhang *et al.* (2021*b*) performed cross-checks on the FCM against the traditional neck region in the joint p.d.f. and found that the threshold derived from the FCM fell within the neck region. These validations confirm that the FCM is consistent with the classical TNTI detection method. As a robust, versatile and convenient method, FCM can also be applied to free-shear flows (Younes *et al.* 2021). Here, the FCM is used to determine the threshold with the following steps.

The ith point in a snapshot has a sequence of measurements $\boldsymbol{\phi_i} = \{\phi_1, \phi_2, \ldots\}$. In the present study, it is selected as the logarithm of the square of the spanwise vorticity, i.e. $\boldsymbol{\phi_i} = \{\lg(\omega_z^2)\}$. The degree of membership, which is denoted by Π_{ij}, represents the probability that the ith data point belongs to the jth cluster. According to the definition, $0 \leqslant \Pi_{ij} \leqslant 1$, and $\sum_{j=1}^{K} \Pi_{ij} = 1$, where K is the number of clusters. In the present study, $K = 2$. The membership degree of each point is calculated in the following way (Bezdec 1981).

(i) Initialize the degree of membership Π_{ij}.

(ii) Calculate the cluster centres

$$c_j = \frac{\sum_{i=1}^{N} \Pi_{ij}^m \phi_i}{\sum_{i=1}^{N} \Pi_{ij}^m}. \tag{4.1}$$

(iii) Update the degree of membership

$$\Pi_{ij} = \frac{1}{\sum_{k=1}^{K} \left(\dfrac{\|\phi_i - c_j\|}{\|\phi_i - c_k\|} \right)^{2/(m-1)}}. \tag{4.2}$$

(iv) Calculate the objective function

$$J_m = \sum_{i=1}^{N} \sum_{j=1}^{K} \Pi_{ij}^m \|\phi_i - c_j\|^2. \tag{4.3}$$

(v) Repeat steps (ii)–(iv) until $|J_m^{(n)} - J_m^{(n-1)}| < 10^{-5}$ or the number of iterations reaches 100.

Here, m is the fuzzy partition matrix exponent to control the degree of fuzzy overlap, with $m > 1$. A larger value of m corresponds to a greater degree of overlap between the clusters. A value of $m = 2$ is taken in the present study. It has been checked that varying m from 1.5 to 2.5 does not influence the conclusions in this paper.

The contour of membership degree $\Pi = 0.5$ can distinguish the turbulent and non-turbulent regions well, but to obtain a clearer physical meaning, the mean value of the enstrophy $\langle \omega_z^2 \rangle_{\Pi=0.5}$ on the contour of $\Pi = 0.5$ is used as the threshold. The threshold obtained by the FCM is compared with the threshold determined by two previous empirical processes. The first method determines the threshold by finding the inflection point of the turbulent region volume (or area) versus the vorticity magnitude threshold curve (Taveira *et al.* 2013; da Silva, Taveira & Borrell 2014*b*). In experiments, a more achievable approach is to plot the slope of the above volume (or area) curve, taking as the threshold the intersection of linear fits to both monotonic variation and nearly constant value regions of the slope curve (Balamurugan *et al.* 2020). The second method takes the inflection point of the conditional average function as the threshold (Prasad & Sreenivasan 1989; Mistry *et al.* 2016; Kohan & Gaskin 2022). The conditional average function is obtained by calculating the area-averaged values across all points inside the region where the local scalar is larger than the given threshold value. In the present study, for a given variable f, the conditional average function is defined as

$$\tilde{f}\,(|\omega_z|_{th}) = \frac{\int (f\,\mathrm{d}a)\,|_{|\omega_z|>|\omega_z|_{th}}}{\int \mathrm{d}a|_{|\omega_z|>|\omega_z|_{th}}}. \tag{4.4}$$

The process of determining the threshold using these two methods in the present study is shown in figure 10. The threshold determined by FCM is compared with the thresholds determined by these two methods. There is not much difference in threshold values among the three methods or between the two jets. These thresholds are located in the region where the area fraction of the turbulent region S_T or conditional average variable $\widetilde{|\omega_z|}$ changes relatively little with the threshold $|\omega_z|_{th}$. This region is not obvious in FOV2 due to the experimental noise, however, the FCM method can still determine the threshold well. Due to the decrease in vorticity in the downstream direction, the threshold determined in FOV2 (figure 10*b*,*d*) is smaller than that in FOV1 (figure 10*a*,*c*) as expected. Considering the vorticity decrease, different thresholds are used to detect the TNTI in FOV1 and FOV2 in the subsequent analysis. Due to identical downstream position of FOV2 and FOV3, an identical threshold is used in FOV3 as in FOV2. In the same FOV, the identical threshold is used in the continuous jet as in the synthetic jet.

Figure 11 shows the instantaneous TNTIs of the continuous and synthetic jets. Hereinafter, the interface spanning across the entire field of view (the 'main' interface) will be the focus. The high-vorticity 'drops' in the non-turbulent region and low-vorticity 'bubbles' in the turbulent region will be ignored.

4.2. *Geometric properties of the TNTI*

As shown in figure 11, the turbulent region of the synthetic jet is wider in the radial position, and the TNTI geometry is more distorted, which indicates that the turbulent region has a larger contact area with the non-turbulent region, which can lead to greater entrainment. In this subsection, the mechanism of the great entrainment of the synthetic jet will be analysed by comparing the geometric properties of the two jets.

The geometric properties of the TNTI analysed in the present study include the radial position y_i and orientation θ_i, as shown in figure 12. The radial position y_i is the distance from the TNTI to the centreline of the jet. The orientation θ_i is the angle between the normal direction of the TNTI and the downstream direction. The sign of θ_i is determined by the right-hand rule, e.g. the angle in figure 12 is negative. The mean value $\overline{y_i}$ and

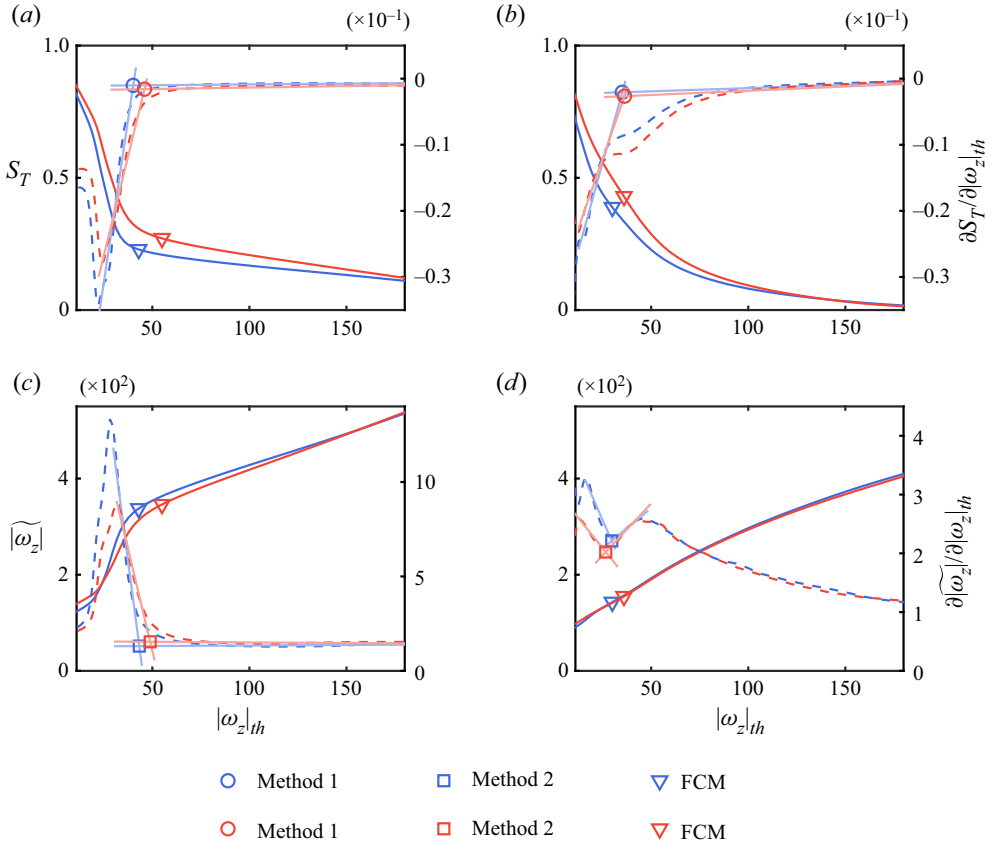

Figure 10. Area fraction of the turbulent region S_T (solid lines, left-hand axis) and derivative $\partial S_T/\partial|\omega_z|_{th}$ (dashed lines, right-hand axis) against $|\omega_z|_{th}$ for (*a*) FOV1 and (*b*) FOV2. The conditional average variable $\widetilde{|\omega_z|}$ (solid lines, left-hand axis) and the derivative $\partial\widetilde{|\omega_z|}/\partial|\omega_z|_{th}$ (dashed lines, right-hand axis) against $|\omega_z|_{th}$ for (*c*) FOV1 and (*d*) FOV2. In each panel, the blue lines and markers represent the continuous jet, and the red lines and markers represent the synthetic jet. The fitting lines are marked by solid lines in light colours. The markers represent the threshold determined using two empirical methods and the FCM method.

standard deviation σ_i of y_i are presented in figure 13(*a*). The $\overline{y_i}$ of the synthetic jet is larger at each downstream position, which indicates that the volume of the synthetic jet turbulent region more rapidly increases. Especially for $10 < x/D < 20$, the growth rate of $\overline{y_i}$ in the synthetic jet is significantly higher. This result is consistent with the position of the largest half-width growth rate in figure 8(*a*). Both results indicate that the entrainment of the synthetic jet is greater in this region. The σ_i of the synthetic jet is also always larger, which can be because the synthetic jet generates a large-scale coherent structure in the near field. To evaluate the scale of the coherent structure, the two-point autocorrelation of the radial fluctuation velocity v' along the TNTI is calculated. The autocorrelation coefficient $R_{v'v'}$ is defined as

$$R_{v'v'}(\Delta s_i) = \frac{\overline{v'(s_i)v'(s_i+\Delta s_i)}}{\sqrt{v'(s_i)v'(s_i)}}, \tag{4.5}$$

where s_i is the curve coordinate along the TNTI. The distributions of $R_{v'v'}$ at different downstream positions are shown in figure 14. The length that corresponds to the point where $R_{v'v'}$ decays to zero is defined as the characteristic length of the large-scale structure.

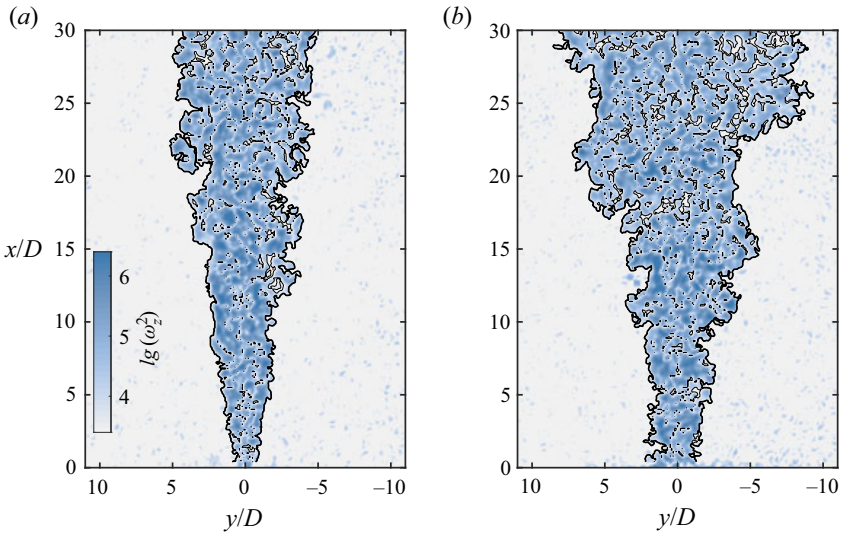

Figure 11. Instantaneous enstrophy fields of the (*a*) continuous jet and (*b*) synthetic jet in logarithmic scaling; the TNTI is denoted by the black solid line.

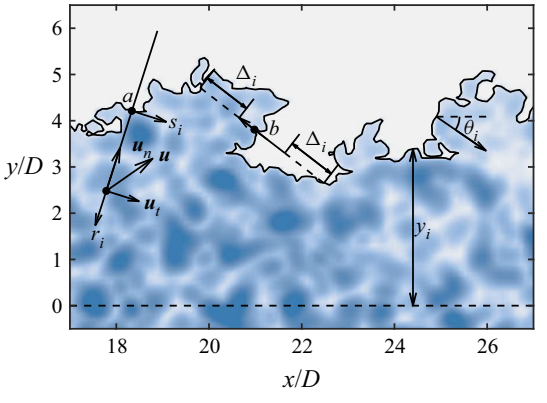

Figure 12. Schematic of the TNTI coordinate system and geometric properties of the TNTI. See §§ 4.2 and 4.4 for details.

At all three sampling locations, the characteristic lengths of the large-scale structure in the synthetic jet are larger, which correspondingly causes greater TNTI fluctuation in the near field, as shown in the standard deviation curve in figure 13. A similar result was reported in the study of Breda & Buxton (2019). They found that the fractal shape orifice suppresses the large-scale coherent structure of the jet, and the radial position of TNTI exhibits a narrower probability density function. Figure 13(*b*) presents $\overline{y_i}$, and σ_i normalized by the local jet half-width $r_{1/2}$. For $0 < x/D < 45$, $\overline{y_i}$ and the σ_i of the synthetic jet are still larger than those of the continuous jet. After the two jets have achieved self-similarity in the far field, the $\overline{y_i}$ in both jets stabilizes at approximately $1.65r_{1/2}$, which is close to the reported result in the far field of a continuous jet ($1.79r_{1/2}$, Mistry *et al.* 2019).

The p.d.f. of the TNTI orientation θ_i on the side of $y/D > 0$ is given in figure 15. For the TNTI on the side of $y/D > 0$, if its shape is smooth, the orientation should be concentrated around -90°. In the near field, the probability density of θ_i in the

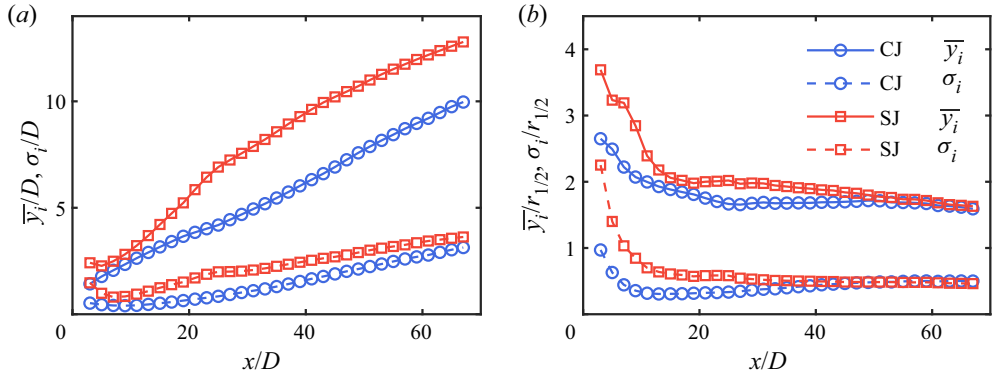

Figure 13. Mean value $\overline{y_i}$ and standard deviation σ_i of the TNTI radial position, normalized by the (*a*) orifice diameter D and (*b*) local jet half-width $r_{1/2}$. For a particular downstream position, $\overline{y_i}$ is obtained by averaging y_i over all frames.

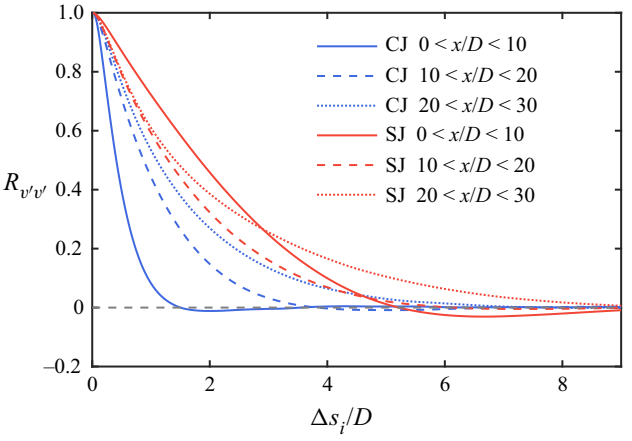

Figure 14. Autocorrelation coefficient $R_{v'v'}$ of the radial fluctuation velocity v' along the TNTI in the three downstream positions of the near field.

synthetic jet is lower at approximately -90°, which indicates a more distorted TNTI. The distorted TNTI of the synthetic jet increases its surface area, which is beneficial for nibbling. With the development of the flow, the p.d.f.s of the TNTI orientation of the two jets develop from a unimodal distribution around -90° to a bimodal distribution with peaks at approximately -50° and -130°. The synthetic and continuous jets form bimodal distributions at approximately $x/D = 35$ and $x/D = 45$, respectively. The positions are consistent with the locations where both jets become self-similar. In the far field, the p.d.f.s of the TNTI orientation are almost identical.Balamurugan *et al.* (2020) also found a bimodal distribution in fully developed mixing layers and attributed it to the influence of large-scale inclined Kelvin–Helmholtz vortical motions. However, in the present study, no similar large-scale vortex structure is observed in the fully developed regions of the jets. The p.d.f.s of the TNTI orientation appear to gradually transform from unimodal to bimodal with the development of the turbulence. Thus, the bimodal distribution can be caused by small-scale turbulent structures. To verify that, the vorticity field is filtered

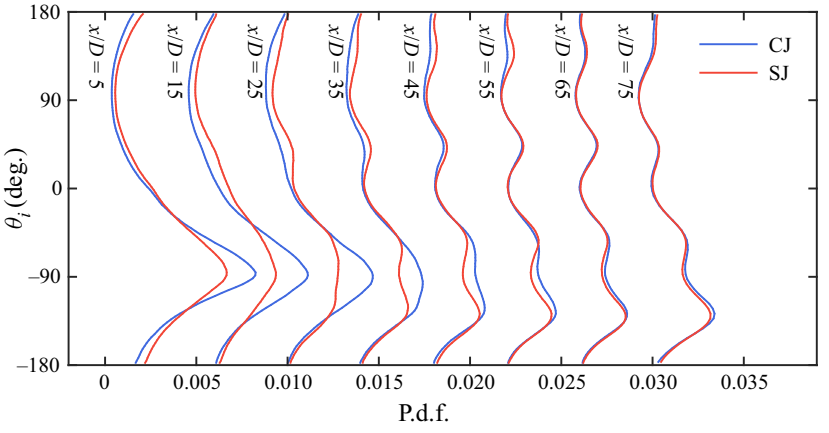

Figure 15. Variations of the p.d.f. of the TNTI orientation on the side of $y/D > 0$. To separate different lines, the profiles are horizontally shifted by 0.004 from the upstream profiles.

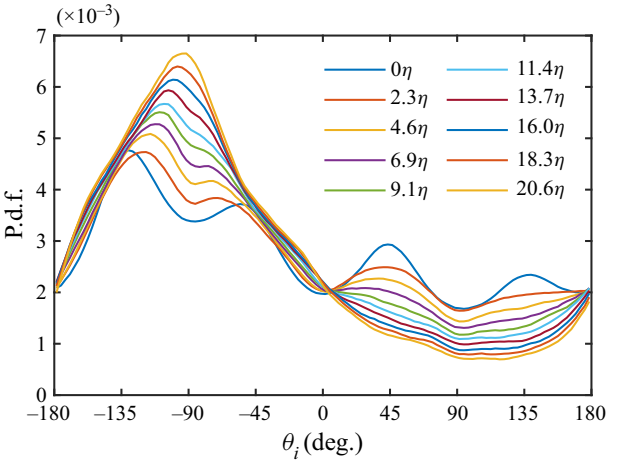

Figure 16. P.d.f. of the TNTI orientation in the far field filtered by filters of different sizes.

using a filter G_Δ of size Δ, i.e. $|\omega_z|_\Delta = |\omega_z| * G_\Delta$. The filter G_Δ of size Δ is defined as

$$G_\Delta(r) = \begin{cases} 0, & |r| \geqslant \Delta/2, \\ 1/\Delta^2, & |r| < \Delta/2. \end{cases} \tag{4.6}$$

The filter size Δ varies from 0, i.e. no filtering, to approximately 20 times Kolmogorov scale η. The p.d.f.s of the TNTI orientation with various Δ values are presented in figure 16. When the filter size increases, the bimodal distribution gradually transforms to a unimodal distribution. When Δ increases to approximately 16η, the p.d.f. of the TNTI orientation completely loses the bimodal distribution character. This size is near the TNTI thickness associated with the enstrophy jump and reported as 15η in the round jet (Wolf *et al.* 2013) and 15.4η–16.8η in the planar jet (Silva, Zecchetto & da Silva 2018). The bimodal distribution originates from small-scale structures near the TNTI with a comparable scale to the thickness of the TNTI.

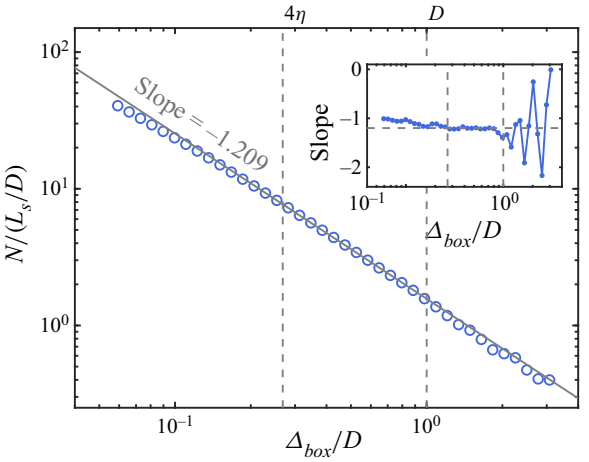

Figure 17. Number N of boxes containing the TNTI as a function of the box size Δ_{box}. Here, $L_s = 5D$ is the streamwise sample width. The grey vertical dashed line represents the upper and lower bounds of the fitting range. The solid grey line represents the straight line fitted with data points within the range. The slope of the fitting line is k. The inset shows the local slope of the points with respect to the box size Δ_{box}.

4.3. *Fractal dimension of the TNTI*

The fractal scaling of the TNTI is important to understand entrainment mechanisms in shear flows. Previous studies have shown that the TNTI exhibits fractal scaling in the turbulent boundary layer (de Silva *et al.* 2013), jet (Mistry *et al.* 2016) and mixing layer (Balamurugan *et al.* 2020). The fractal reflects that the deformations caused by a hierarchy of eddies in the turbulent inertial range (de Silva *et al.* 2013). The fractal is usually characterized by the fractal dimension D_f. The above studies have found that the TNTI has a fractal dimension $D_f = 2.3$–2.4 in fully developed turbulence. This result is consistent with the theoretical value $D_f = 2 + 1/3$ derived by Sreenivasan, Ramshankar & Meneveau (1989) based on the Reynolds number similarity and Kolmogorov scalings. In the study of axisymmetric jets, Mistry, Dawson & Kerstein (2018) found that the fractal dimension of TNTI gradually increased from $D_f \approx 2$ near the orifice to $D_f \approx 2.33$ at the end of the potential core. Breda & Buxton (2019) found that the TNTI exhibited a non-equilibrium scaling of $D_f = 1 + 6/5$ and a Kolmogorov scaling of $D_f = 1 + 4/3$ in the near and far fields of fractal orifice jets, respectively. They suggested that further downstream locations were necessary to unveil the transition from non-equilibrium scaling to Kolmogorov scaling.

The fractal dimension of the TNTI can be obtained by the box-counting technique (Sreenivasan *et al.* 1989; de Silva *et al.* 2013; Mistry *et al.* 2016; Wu *et al.* 2019; Balamurugan *et al.* 2020; Li *et al.* 2020). The fractal dimension D_2 of the intersection between the TNTI and the x–y plane is calculated, and the fractal dimension of the TNTI can be obtained by $D_f = D_2 + 1$ (Mandelbrot 1982). Boxes are used to cover the flow field; the number N of boxes containing the TNTI and box size Δ_{box} follow the power law of $N \sim \Delta_{box}^{k}$. The fractal dimension can be estimated as $D_2 = -k$, where k is the slope of function $N(\Delta_{box})$ in a log-log plot. Considering the requirement for calculating the fractal dimension and evolution of the fractal dimension, the fractal dimension of the TNTI in the range of $x \pm 2.5D$ is taken as the fractal dimension at x. As shown in figure 17, N increases when the box size Δ_{box} decreases, which is approximately a straight line in the log-log plot. The local slope of the line does not converge in the large-scale

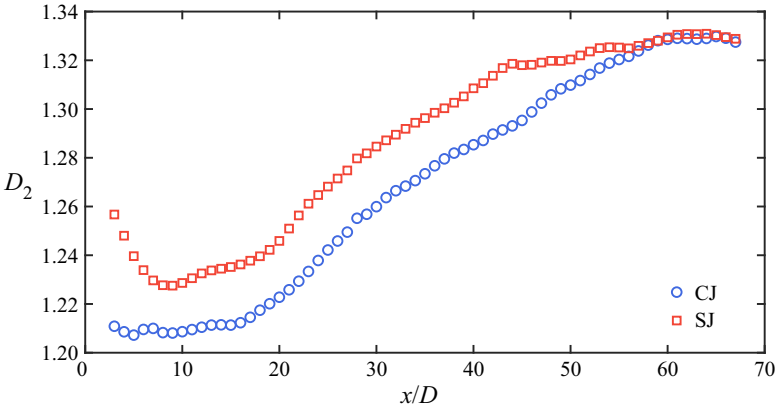

Figure 18. Downstream evolutions of the fractal dimension D_2.

region due to the small sample number of boxes, while it approaches -1 in the small-scale region because the box size is close to the experimental resolution and Kolmogorov scale. Therefore, the fractal dimension of the TNTI is obtained by fitting the data points in the region of $4\eta - D$, where the local slope is relatively stable. As shown in figure 18, both TNTI fractal dimensions D_2 of the two jets reach 1.33 in the far field, which is consistent with previous studies (de Silva *et al.* 2013; Mistry *et al.* 2016; Balamurugan *et al.* 2020). In the range of $0 < x/D < 15$, $D_2 \approx 1.21$ for the continuous jet, which is close to $D_2 \approx 1.2$ reported in the non-equilibrium dissipation turbulence (Zhou & Vassilicos 2017). Then, D_2 gradually increases to a constant value in the far field. Before reaching the constant value, the synthetic jet has a higher D_2, which implies that the synthetic jet has a larger TNTI surface area under the condition of identical characteristic scale. Furthermore, D_2 of the synthetic jet rapidly decreases for $0 < x/D < 10$. The position where D_2 reduces to a minimum value basically coincides with the position where the large-scale vortex structure breaks down, as shown in figure 5. The decrease in fractal dimension can be related to the fact that the vortex ring of the synthetic jet increases the two-dimensionality of the flow, while the collapse of the vortex ring enhances the three-dimensionality of the flow for $x/D > 10$.

4.4. *Conditional average profiles near the TNTI*

The TNTI is highly distorted, and it is difficult for the Cartesian coordinate system in figure 3 to describe the variations of physical quantities on both sides of the TNTI. Therefore, a TNTI coordinate system is taken for each point at the TNTI (see the coordinate a in figure 12). The direction of the r_i axis is given by the normal direction of the TNTI $\boldsymbol{n} = \nabla\omega_z/|\omega_z|$. The scalars are conditionally averaged over distance r_i from the TNTI over all snapshots, denoted by $\langle\cdot\rangle$. The velocity $\boldsymbol{u}$ can be decomposed into normal velocity $\boldsymbol{u_n}$ and tangential velocity $\boldsymbol{u_t}$, as shown in figure 12. Due to the wrinkled nature of the TNTI, some coordinates may cross the TNTI multiple times (see the coordinate b in figure 12). Following Watanabe *et al.* (2018), the data points that are too close to the second cross-point are discarded, and only the part with a distance of $\Delta_i > 20\eta$ from the second cross-point is selected for the conditional average. It is checked that varying Δ_i from 15η to 25η does not influence the conclusions in this paper.

The enstrophy is conditionally averaged to evaluate the small-scale motions near the TNTI, as shown in figure 19. For the two jets, the enstrophy is virtually zero in the

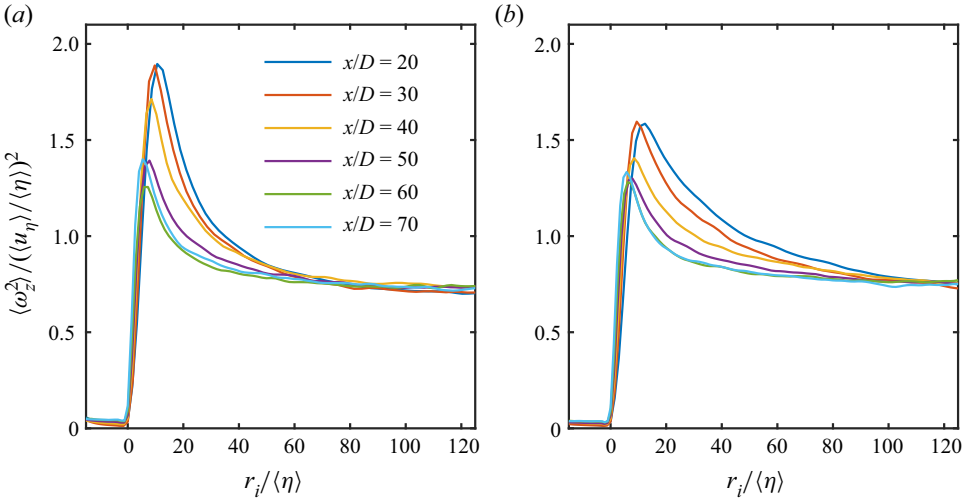

Figure 19. Conditional average profiles of enstrophy in the (*a*) continuous jet and (*b*) synthetic jet. The profiles are normalized by the local conditional average Kolmogorov velocity and length scale, i.e. $(\langle u_\eta\rangle/\langle\eta\rangle)^2$.

non-turbulent region and tends to a constant value in the turbulent core region after a sharp jump. The enstrophy jump thickness of 10η–20η is consistent with previous studies (Wolf *et al.* 2013; Silva *et al.* 2018). In the far field, the enstrophy profiles of both jets collapse to a shape close to the unified profile described by Zecchetto & da Silva (2021), although the constant enstrophy value is less than 1 in the turbulent core region due to the absence of two vorticity components. Thus, the two jets achieve the universality of small-scale motions in the far field, although they are quite different in the near field. The deviation of normalized enstrophy from the constant value in the turbulent core region can be attributed to a deviation of the flow from the homogeneity (Zecchetto & da Silva 2021). In the near field, the normalized enstrophy of the synthetic jet is adjusted from the peak of the jump to a constant value after a longer distance, which implies that there are stronger local inhomogeneity and intense vortices near the TNTI of the synthetic jet.

The conditional average profiles of the normal velocity relative to the TNTI, which are denoted by $[\langle u_n\rangle - \langle u_n(0)\rangle]$, are shown in figure 20(*a*). For $x/D > 10$, $[\langle u_n\rangle - \langle u_n(0)\rangle]$ is positive in the non-turbulent region and negative in the turbulent region, which implies that fluid from both sides of the TNTI is transported towards the TNTI. Similar profiles, known as the counterflow profile, have been observed in a previous study (Mistry *et al.* 2019) and found to correlate well with the local entrainment. By conditionally averaging the normal velocity profile based on the local entrainment velocity, Mistry *et al.* (2019) found that the normal velocity gradient $\partial\langle u_n\rangle/\partial r_i$ was larger in the local entrainment region than in the local detrainment region. They argued that the intense Taylor-scale structures along the TNTI generated a compressive strain field normal to the TNTI. The compressive strain field increases the enstrophy production and promotes local entrainment. In the present study, for $10 < x/D < 45$, the range after the synthetic jet vortex rings have broken down and before the far field, the $[\langle u_n\rangle - \langle u_n(0)\rangle]$ of the synthetic jet exhibits a larger gradient, which can be confirmed in figure 20(*b*). It could be inferred that there are stronger vortices near the TNTI in the synthetic jet to promote entrainment.

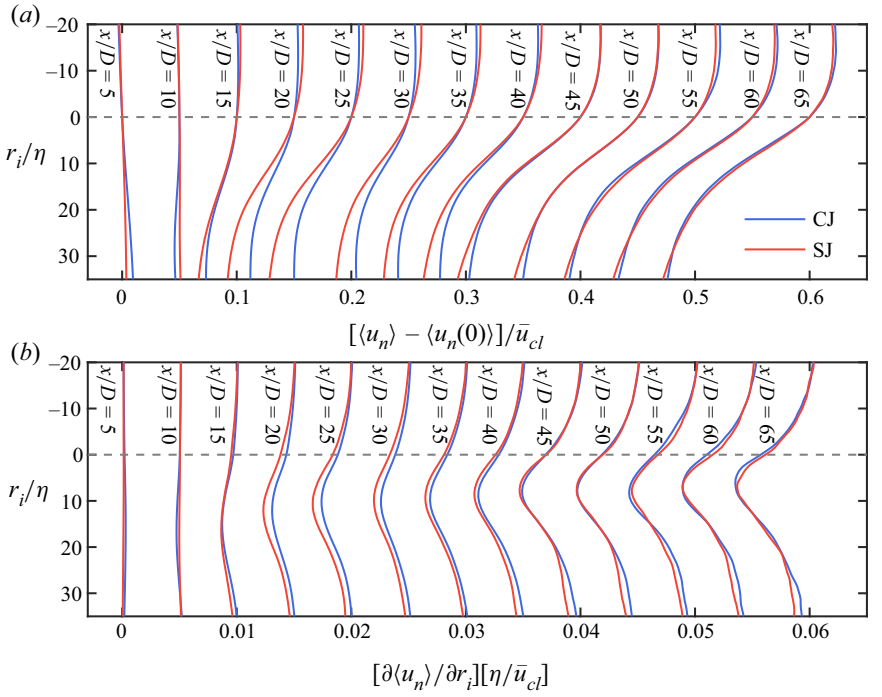

Figure 20. (*a*) Variations in the conditional average profiles of the normal velocity $\langle u_n\rangle$ relative to TNTI. Here, $\langle u_n(0)\rangle$ is the local fluid normal velocity at the TNTI, the position where $r_i = 0$. To separate different lines, the profiles are horizontally shifted by 0.05 from the upstream profiles. (*b*) Variations in the gradient of $\langle u_n\rangle$, i.e. $\partial\langle u_n\rangle/\partial r_i$. To separate different lines, the profiles are horizontally shifted by 0.005 from the upstream profiles.

4.5. *Entrainment analysis: engulfment*

Engulfment is the process where the irrotational fluid is drawn into the turbulent region due to inviscid motions, which is one of the mechanisms of entrainment. Whether the enhancement of large-scale structures by synthetic jets increases the contribution of engulfment will be analysed in this subsection.

There are many irrotational bubbles in the turbulent region, as shown in figure 11, but not all of these bubbles are generated by engulfment. da Silva *et al.* (2014*b*) compared the p.d.f.s of the bubble scale in jets and homogeneous turbulence and found that both followed the -3 power law. Jahanbakhshi & Madnia (2016) used Taylor scale as the border to divide the irrotational bubbles into two categories: those near the TNTI and those far away from the TNTI. They found that the p.d.f. of the former was close to the -4 power law, while the latter followed the -3 power law. The bubbles near the TNTI can be considered to be generated by engulfment, while the bubbles in the turbulent core region are not related to the engulfment. In the present study, bubbles are divided by the homogeneity of their internal flow field. The velocity standard deviation within the bubble is defined as

$$\sigma_b = \sqrt{\overline{(u - \langle u\rangle_b)^2}}, \tag{4.7}$$

where $\langle u\rangle_b$ is the mean velocity within the bubble. The variations in σ_b with the distance from the TNTI are shown in figure 21(*a*). When the irrotational fluid is only drawn into the turbulent region to form engulfed bubbles, σ_b in the engulfed bubble is low, which implies that a relatively uniform flow is maintained in the engulfed bubble. When the engulfed

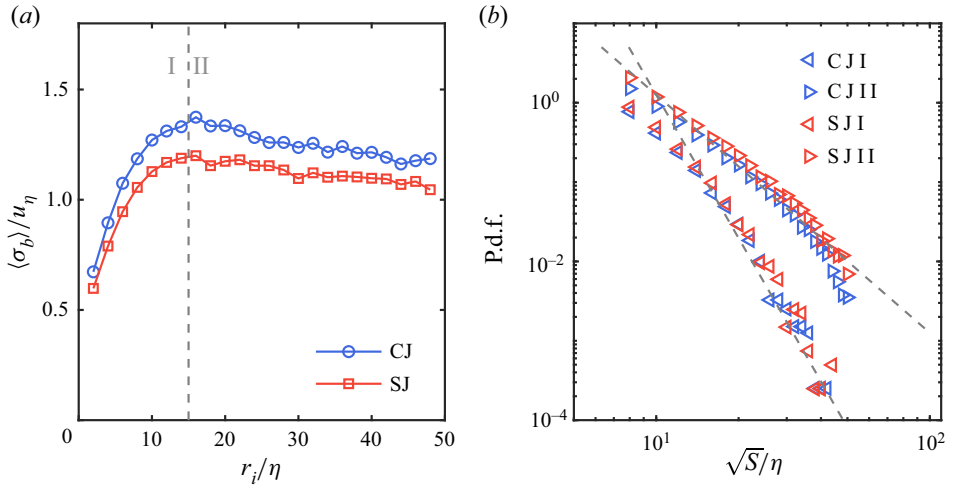

Figure 21. (*a*) Conditional average profiles of the velocity standard deviation within the bubble. The velocity standard deviation is normalized by the Kolmogorov velocity scale u_η. (*b*) P.d.f.s of the bubble scale, represented by the square root of the bubble area S.

bubble enters the turbulent core region, the fluid in the engulfed bubble gradually becomes turbulent. The σ_b gradually increases and subsequently remains almost constant. However, the homogeneities in the turbulent bubbles should be identical regardless of the distance from the TNTI. According to the trend of σ_b in figure 21(*a*), the bubbles are divided into region I and region II with 15η as the border. The p.d.f.s of the bubble scale in the two regions are shown in figure 21(*b*). The p.d.f.s of the bubble scale in region II still follow the -3 power law, while those in region I are closer to the -6 power law. This result is smaller than the -4 power obtained by Jahanbakhshi & Madnia (2016) in the compressible mixing layer at Mach number 0.2. In the four studied cases with convective Mach numbers of 0.2–1.8, the engulfed bubble only exhibits the -4 power law distribution in the case with Mach number 0.2, while it exhibits the -3 power law distribution in the rest of the cases. Since the Mach number in the present study is much less than 0.2, the difference in results can be due to the effect of compressibility. Combining the results of figure 21(*a*,*b*), the bubbles in region I are closely related to the engulfment, while the bubbles in region II are most likely generated in the turbulent core region. Subsequent analysis will only count the bubbles in region I.

The contribution of engulfment can be estimated from the volume of the bubble using similar methods to Westerweel *et al.* (2009) and Jahanbakhshi & Madnia (2016). Assuming that the bubbles within 15η of the TNTI are generated by engulfment and exhibit symmetry with respect to the centreline of the jet, the engulfment flow rate Q_e can be estimated by

$$Q_e = 2\pi \int_0^{r_0} \overline{u(r)}p(r)r\,\mathrm{d}r, \tag{4.8}$$

where $p(r)$ is the probability that the vorticity at the point is lower than the threshold. The result shows that the contribution of engulfment in the two jets, i.e. Q_e/Q^*, is less than 4 %, which is close to the results 4 %–8 % in previous studies (Westerweel *et al.* 2005, 2009; Jahanbakhshi & Madnia 2016; Long, Wang & Pan 2022). Thus, engulfment is not the dominant mechanism in the entrainment process of the synthetic jet, as in the cases of continuous jets and turbulent boundary layers. Due to the 2-D PIV data, some

intersections of the measurement plane and low-vorticity structures that are connected to the non-turbulent region will be identified as bubbles. This issue may overestimate the bubble contribution to entrainment but does not affect the above conclusion.

5. Conclusion

In this paper, the synthetic and continuous jets at $Re_j = 3150$ were measured using the 2-D PIV technique. The fuzzy clustering method appropriately determined the vorticity threshold in the region where the area fraction of the turbulent region varied relatively little with the threshold, and the TNTI was detected by the threshold. The TNTI properties of the two jets were investigated, and the following conclusions are drawn.

The difference between the two jets in entrainment coefficient and TNTI properties mainly occurs in the near field. The entrainment coefficient of the synthetic jet is higher in the near field, while it is constant and equal to that of the continuous jet after achieving self-similarity in the far field. In the synthetic jet, the turbulent kinetic energy is enhanced by the breakdown of the vortex ring, and the first component of the entrainment coefficient correspondingly increases. Therefore, the maximum entrainment coefficient appears after the complete breakdown of the vortex ring, which indicates that the 'breakdown of the vortex ring' enhances the entrainment in the present synthetic jet. The TNTIs of the two jets have different geometric and dynamic properties in the near field. For the geometric properties, the TNTI of the synthetic jet exhibits larger mean value and fluctuation of radial position, a wider p.d.f. of orientation and a larger fractal dimension. The results show that the TNTI of the synthetic jet has a more distorted shape and a larger surface area, which enhance the nibbling process. For the dynamic properties, $\partial\langle u_n\rangle/\partial r_i$ of the synthetic jet is larger, which has been confirmed in previous studies to promote the generation of enstrophy. In the far field, the two jets tend to have identical TNTI properties, the TNTI fractal dimensions D_f are constant at approximately 2.33 and $\partial\langle u_n\rangle/\partial r_i$ of the jets are almost equal.

The bimodal distribution of the TNTI orientation in the fully developed region is related to the TNTI thickness-scale structure. The p.d.f.s of the TNTI orientation in the two jets transform from the unimodal distribution around -90° in the near field to the bimodal distribution with peaks at approximately -50° and -130° in the far field. The multi-scale analysis shows that the bimodal distribution is related to the small-scale structure whose size is comparable to the thickness of the TNTI, which is a different mechanism from the conclusion of a previous study that the bimodal distribution originates from a large-scale structure.

Engulfment is not the dominant mechanism of entrainment in the synthetic jet. The engulfment contribution in the synthetic jet is estimated by counting the bubble probability and calculating the engulfment flow rate. The result shows that the engulfment contribution in the present synthetic jet does not exceed 4 %, which is close to that of the continuous jet. An identical conclusion was obtained in previous studies of continuous jets and mixing layers.

Funding. This work was supported by the National Natural Science Foundation of China (grant numbers 91852206, 11721202).

Declaration of interests. The authors report no conflict of interest.

Author ORCIDs.
Congyi Xu https://orcid.org/0000-0003-1093-7561;
Yanguang Long https://orcid.org/0000-0002-8201-9308;
Jinjun Wang https://orcid.org/0000-0001-9523-7403.

References

Balamurugan, G., Rodda, A., Philip, J. & Mandal, A.C. 2020 Characteristics of the turbulent non-turbulent interface in a spatially evolving turbulent mixing layer. *J. Fluid Mech.* **894**, A4.

Bezdec, J.C. 1981 *Pattern Recognition with Fuzzy Objective Function Algorithms*. Plenum.

Bisset, D.K., Hunt, J.C.R. & Rogers, M.M. 2002 The turbulent/non-turbulent interface bounding a far wake. *J. Fluid Mech.* **451**, 383–410.

Breda, M. & Buxton, O.R.H. 2017 Near and far-field analysis of an axisymmetric fractal-forced turbulent jet. In *Progress in Turbulence VII* (ed. R. Örlü, A. Talamelli, M. Oberlack & J. Peinke), pp. 211–217. Springer.

Breda, M. & Buxton, O.R.H. 2018 Influence of coherent structures on the evolution of an axisymmetric turbulent jet. *Phys. Fluids* **30** (3), 035109.

Breda, M. & Buxton, O.R.H. 2019 Behaviour of small-scale turbulence in the turbulent/non-turbulent interface region of developing turbulent jets. *J. Fluid Mech.* **879**, 187–216.

Cao, S., Li, Y., Zhang, J. & Deguchi, Y. 2019 Lagrangian analysis of mass transport and its influence on the lift enhancement in a flow over the airfoil with a synthetic jet. *Aerosp. Sci. Technol.* **86**, 11–20.

Cater, J.E. & Soria, J. 2002 The evolution of round zero-net-mass-flux jets. *J. Fluid Mech.* **472**, 167–200.

Champagnat, F., Plyer, A., Le Besnerais, G., Leclaire, B., Davoust, S. & Le Sant, Y. 2011 Fast and accurate PIV computation using highly parallel iterative correlation maximization. *Exp. Fluids* **50** (4), 1169–1182.

Chauhan, K., Philip, J., de Silva, C.M., Hutchins, N. & Marusic, I. 2014 The turbulent/non-turbulent interface and entrainment in a boundary layer. *J. Fluid Mech.* **742**, 119–151.

Eri, Q.T., Hong, L., Li, T., Wang, Q. & Wang, M.J. 2016 Numerical simulations of mixing enhancement in subsonic jet using high-momentum synthetic jets. *J. Propul. Power* **32** (5), 1095–1103.

Glezer, A. & Amitay, M. 2002 Synthetic jets. *Annu. Rev. Fluid Mech.* **34** (1), 503–529.

Hussein, H.J., Capp, S.P. & George, W.K. 1994 Velocity measurements in a high-Reynolds-number, momentum-conserving, axisymmetric, turbulent jet. *J. Fluid Mech.* **258**, 31–75.

Jahanbakhshi, R. & Madnia, C.K. 2016 Entrainment in a compressible turbulent shear layer. *J. Fluid Mech.* **797**, 564–603.

James, R.D., Jacobs, J.W. & Glezer, A. 1996 A round turbulent jet produced by an oscillating diaphragm. *Phys. Fluids* **8** (9), 2484–2495.

Kohan, K.F. & Gaskin, S.J. 2022 On the scalar turbulent/turbulent interface of axisymmetric jets. *J. Fluid Mech.* **950**, A32.

Krishan, G., Aw, K.C. & Sharma, R.N. 2019 Synthetic jet impingement heat transfer enhancement – a review. *Appl. Therm. Engng* **149**, 1305–1323.

Li, S., Wu, D., Cui, G. & Wang, J. 2020 Experimental study on properties of turbulent/non-turbulent interface over riblets surfaces at low Reynolds numbers. *Chin. J. Theor. Appl. Mech.* **52** (6), 1632–1644.

Long, Y., Wang, J. & Pan, C. 2022 Universal modulations of large-scale motions on entrainment of turbulent boundary layers. *J. Fluid Mech.* **941**, A68.

Long, Y.G., Wu, D. & Wang, J.J. 2021 A novel and robust method for the turbulent/non-turbulent interface detection. *Exp. Fluids* **62** (7), 138.

Mallinson, S.G., Hong, G. & Reizes, J. 1999 Some characteristics of synthetic jets. In *30th AIAA Fluid Dynamics Conference, Norfolk, VA, USA,* AIAA Paper 1999-3651. American Institute for Aeronautics and Astronautics.

Mallinson, S.G., Reizes, J.A. & Hong, G. 2001 An experimental and numerical study of synthetic jet flow. *Aeronaut. J.* **105** (1043), 41–49.

Mandelbrot, B.B. 1982 *The Fractal Geometry Of Nature*. Freeman.

Mathew, J. & Basu, A.J. 2002 Some characteristics of entrainment at a cylindrical turbulence boundary. *Phys. Fluids* **14** (7), 2065–2072.

Mistry, D., Dawson, J.R. & Kerstein, A.R. 2018 The multi-scale geometry of the near field in an axisymmetric jet. *J. Fluid Mech.* **838**, 501–515.

Mistry, D., Philip, J. & Dawson, J.R. 2019 Kinematics of local entrainment and detrainment in a turbulent jet. *J. Fluid Mech.* **871**, 896–924.

Mistry, D., Philip, J., Dawson, J.R. & Marusic, I. 2016 Entrainment at multi-scales across the turbulent/non-turbulent interface in an axisymmetric jet. *J. Fluid Mech.* **802**, 690–725.

Paillat, S. & Kaminski, E. 2014 Entrainment in plane turbulent pure plumes. *J. Fluid Mech.* **755**, R2.

Pan, C., Wang, H.P. & Wang, J.J. 2013 Phase identification of quasi-periodic flow measured by particle image velocimetry with a low sampling rate. *Meas. Sci. Technol.* **24** (5), 055305.

PAN, C., XUE, D., XU, Y., WANG, J.J. & WEI, R.J. 2015 Evaluating the accuracy performance of Lucas–Kanade algorithm in the circumstance of PIV application. *Sci. China Phys. Mech. Astron.* **58** (10), 104704.

PANCHAPAKESAN, N.R. & LUMLEY, J.L. 1993 Turbulence measurements in axisymmetric jets of air and helium. Part 1. Air jet. *J. Fluid Mech.* **246**, 197–223.

POPE, S.B. 2000 *Turbulent Flows*. Cambridge University Press.

PRASAD, R.R. & SREENIVASAN, K.R. 1989 Scalar interfaces in digital images of turbulent flows. *Exp. Fluids* **7** (4), 259–264.

VAN REEUWIJK, M. & CRASKE, J. 2015 Energy-consistent entrainment relations for jets and plumes. *J. Fluid Mech.* **782**, 333–355.

REUTHER, N. & KAHLER, C.J. 2018 Evaluation of large-scale turbulent/non-turbulent interface detection methods for wall-bounded flows. *Exp. Fluids* **59** (7), 121.

SHUSTER, J.M. & SMITH, D.R. 2007 Experimental study of the formation and scaling of a round synthetic jet. *Phys. Fluids* **19** (4), 045109.

DA SILVA, C.B., HUNT, J.C.R., EAMES, I. & WESTERWEEL, J. 2014*a* Interfacial layers between regions of different turbulence intensity. *Annu. Rev. Fluid Mech.* **46** (1), 567–590.

DE SILVA, C.M., PHILIP, J., CHAUHAN, K., MENEVEAU, C. & MARUSIC, I. 2013 Multiscale geometry and scaling of the turbulent-nonturbulent interface in high Reynolds number boundary layers. *Phys. Rev. Lett.* **111** (4), 044501.

DA SILVA, C.B., TAVEIRA, R.R. & BORRELL, G. 2014*b* Characteristics of the turbulent/nonturbulent interface in boundary layers, jets and shear-free turbulence. *J. Phys.: Conf. Ser.* **506**, 012015.

SILVA, T.S., ZECCHETTO, M. & DA SILVA, C.B. 2018 The scaling of the turbulent/non-turbulent interface at high Reynolds numbers. *J. Fluid Mech.* **843**, 156–179.

SMITH, B.L. & GLEZER, A. 1998 The formation and evolution of synthetic jets. *Phys. Fluids* **10** (9), 2281–2297.

SMITH, B.L. & SWIFT, G.W. 2003 A comparison between synthetic jets and continuous jets. *Exp. Fluids* **34** (4), 467–472.

SREENIVASAN, K.R., RAMSHANKAR, R. & MENEVEAU, C. 1989 Mixing, entrainment and fractal dimensions of surfaces in turbulent flows. *Proc. R. Soc. Lond.* A **421** (1860), 79–108.

TAVEIRA, R.R., DIOGO, J.S., LOPES, D.C. & DA SILVA, C.B. 2013 Lagrangian statistics across the turbulent-nonturbulent interface in a turbulent plane jet. *Phys. Rev.* E **88** (4), 043001.

TURNER, J.S. 1986 Turbulent entrainment: the development of the entrainment assumption, and its application to geophysical flows. *J. Fluid Mech.* **173**, 431–471.

WATANABE, T., SAKAI, Y., NAGATA, K., ITO, Y. & HAYASE, T. 2015 Turbulent mixing of passive scalar near turbulent and non-turbulent interface in mixing layers. *Phys. Fluids* **27** (8), 085109.

WATANABE, T., ZHANG, X. & NAGATA, K. 2018 Turbulent/non-turbulent interfaces detected in DNS of incompressible turbulent boundary layers. *Phys. Fluids* **30** (3), 035102.

WESTERWEEL, J., FUKUSHIMA, C., PEDERSEN, J.M. & HUNT, J.C. 2005 Mechanics of the turbulent-nonturbulent interface of a jet. *Phys. Rev. Lett.* **95** (17), 174501.

WESTERWEEL, J., FUKUSHIMA, C., PEDERSEN, J.M. & HUNT, J.C.R. 2009 Momentum and scalar transport at the turbulent/non-turbulent interface of a jet. *J. Fluid Mech.* **631**, 199–230.

WOLF, M., HOLZNER, M., LUTHI, B., KRUG, D., KINZELBACH, W. & TSINOBER, A. 2013 Effects of mean shear on the local turbulent entrainment process. *J. Fluid Mech.* **731**, 95–116.

WU, D., WANG, J.J., CUI, G.Y. & PAN, C. 2019 Effects of surface shapes on properties of turbulent/non-turbulent interface in turbulent boundary layers. *Sci. China Technol. Sci.* **63** (2), 214–222.

YOUNES, K., GIBEAU, B., GHAEMI, S. & HICKEY, J.P. 2021 A fuzzy cluster method for turbulent/non-turbulent interface detection. *Exp. Fluids* **62** (4), 73.

ZECCHETTO, M. & DA SILVA, C.B. 2021 Universality of small-scale motions within the turbulent/non-turbulent interface layer. *J. Fluid Mech.* **916**, A9.

ZHANG, B.L., LIU, H., LI, Y.Y., LIU, H. & DONG, J.Z. 2021*a* Experimental study of coaxial jets mixing enhancement using synthetic jets. *Appl. Sci. Basel* **11** (2), 803.

ZHANG, H.Y., RIVAL, D.E. & WU, X.H. 2021*b* Kinematics of the turbulent and nonturbulent interfaces in a subsonic airfoil flow. *AIAA J.* **59** (6), 2155–2168.

ZHOU, J., ADRIAN, R.J., BALACHANDAR, S. & KENDALL, T.M. 1999 Mechanisms for generating coherent packets of hairpin vortices in channel flow. *J. Fluid Mech.* **387**, 353–396.

ZHOU, Y. & VASSILICOS, J.C. 2017 Related self-similar statistics of the turbulent/non-turbulent interface and the turbulence dissipation. *J. Fluid Mech.* **821**, 440–457.

ZONG, H., VAN PELT, T. & KOTSONIS, M. 2018 Airfoil flow separation control with plasma synthetic jets at moderate Reynolds number. *Exp. Fluids* **59** (11), 169.